Laser-Controlled Dissociation of $C_2H_2^{2+}$: Ehrenfest Dynamics Using Time-Dependent Density Functional Theory

Wenkel Liang, Christine M. Isborn, and Xiaosong Li*

University of Washington, Department of Chemistry, Box 351700, Seattle, Washington 98195-1700

Received: December 26, 2008; Revised Manuscript Received: February 16, 2009

Intense laser field dissociations of the acetylene dication $C_2H_2^{2+}$ are studied by an *ab initio* Ehrenfest dynamics method with time-dependent density functional theory. Various field frequencies (9.5∼13.6 eV) and field directions are applied to a Boltzmann ensemble of $C_2H_2^{2+}$ molecules. With the laser field perpendicular to the molecular axis, four fragmentation channels are observed at high frequency with no dominant pathway. With the field parallel to the molecular axis, fragmentations occur at all frequencies and the amount of C−H bond breakage increases with laser frequency. Selective dissociation patterns are observed with low-frequency fields parallel to the molecular axis. A systematic analysis of excited-state potential energy surfaces is used to rationalize the simulation results.

I. Introduction

Laser technology and methodology have undergone a rapid development in the past decade. The seminal work of scientists such as Zewail and co-workers,[1] as recognized by the Nobel Prize in 1999, has extended the role of lasers in chemistry from a static probe used for obtaining accurate spectra to a dynamic tool that can reveal and even control time-resolved chemical reactions. Advanced laser techniques, such as ultrashort (femtosecond and subpicosecond) laser pulses, high-intensity electric fields, pulse tailoring, and multiwave mixing, provide increasing control of molecular electronic and vibrational behavior.[2,3] These recent advances provide inspiration to scientists in devising electromagnetic fields that control the outcome of a chemical reaction via a desired pathway. Laser beams are now being used as optical tweezers to rotate DNA molecules to desired alignment,[4] to control bond cleavage,[5] to enhance photon transitions,[6−9] to prepare molecules in selected vibrational excited states,[10,11] and to induce desorption processes on surfaces.[12−16] Controllable photochemistry will undoubtedly have a far-reaching impact in industry, public health, environmental improvement, atmospheric restoration, and alternative energy research.

While innovative experimental techniques for controlling reactions with lasers are now applied to bond selective chemistry (for recent reviews, see refs 17 and 18), the underpinnings of many laser-controlled mechanisms still remain unclear. Although potential energy surface (PES) analysis provides a starting point for understanding laser-controlled molecular reactions, the detailed control mechanism is very difficult to obtain even for small molecules. The laser pulse can "dress" the PESs, causing time-dependent shifts in PES energy (Stark shifts) and shape. Direct electron−nuclear dynamics with laser pulse effects are necessary for understanding how the PESs involved in the dissociation reactions are accessed with various fields. In a high-intensity laser field, perturbative calculations are no longer valid to describe the electronic dynamics, which often involve multiple PESs. Such electronic nonadiabaticity can be treated in an exact way by solving the time-dependent Schrodinger equation (TDSE) simultaneously for both electrons and nuclei. However, explicit numerical integration of the full TDSE is computationally prohibitive. Our recent development of *ab initio* Ehrenfest dynamics with TDHF and TDDFT offers an affordable solution by propagating classical trajectories for molecules on an average nonadiabatic PES.[19] This approach has been used to study nonadiabatic electronic response and surface collisions.

The goal of this study is to understand some aspects of laser control mechanism. Toward this effort, we use real-time quantum electron dynamics with a variety of photon energies and electric field orientations, along with PES analysis of various reaction pathways, for strategic controls with the photon energy and orientation of the electric field. With the support of this work, we can also demonstrate that our recently developed *ab initio* nonadiabatic Ehrenfest dynamics technique can be used to simulate and understand laser-controlled dissociation, as we now include the effects of an applied laser field within our dynamics. In this paper, we present theoretical insights to laser-controlled reactions via a coherent frequency control scheme by examining the results of the Ehrenfest/TDDFT method applied to the dissociation of the acetylene dication ($C_2H_2^{2+}$). The acetylene dication has attracted great interest in both experiments[20−22] and theoretical calculations,[23−29] because of its importance as a prototype of H^+ migration, and because it is one of the smallest stable polyatomic dications. To simulate $C_2H_2^{2+}$ interacting with an applied laser field, we use our nonadiabatic Ehrenfest/TDDFT dynamics and include the effects of a field within the electric dipole approximation. We rationalize our results with PES analysis, showing how the results of various applied field directions and frequencies are the result of accessing particular PESs. The combined techniques of nonadiabatic dynamics and PES analysis provide insight into possible control schemes and also aid in understanding the nuances of a photoinduced dissociation.

II. Method

A. Ab Initio Direct Ehrenfest Dynamics. We use our *ab initio* direct Ehrenfest dynamics in this study. The electronic degrees of freedom are propagated with real-time TDDFT/TDHF, which has proven to be able to realistically simulate electron-field interactions, while the electron−nuclear nonadiabatic interactions are modeled with the Ehrenfest technique, which propagates the nuclei on the mean-field electronic potential. This method has recently been used to model the

10.1021/jp811431u CCC: $40.75
Published on Web 03/25/2009

collisions of oxygen with graphite.[30] We here present a brief summary of the methodology; for detailed machinery and in-depth discussion about the algorithm, we refer readers to refs 19, 30, and 31.

The *ab initio* direct Ehrenfest dynamics is implemented with a triple-split operator scheme with three different integrators: nuclear velocity-Verlet,[32] a nuclear position coupled midpoint Fock/Kohn−Sham integrator, and a modified midpoint and unitary transformation (MMUT) TDHF/TDDFT. All energies, gradients, and properties are generated directly as needed, or "on the fly".

The electronic degrees of freedom are propagated with a MMUT.[19] The unitary transformation matrix is a time-evolution operator constructed from the eigenvectors $\mathbf{C}(t_k)$ and eigenvalues $\varepsilon(t_k)$ of the Fock/Kohn−Sham matrix

$$\mathbf{C}^{\dagger}(t_k)\cdot\mathbf{K}(t_k)\cdot\mathbf{C}(t_k) = \varepsilon(t_k) \tag{1}$$

$$\begin{aligned}\mathbf{U}(t_k) &= \exp[i\cdot 2\Delta t_e\cdot\mathbf{K}(t_k)] \\ &= \mathbf{C}(t_k)\cdot\exp[i\cdot 2\Delta t_e\cdot\varepsilon(t_k)]\cdot\mathbf{C}^{\dagger}(t_k)\end{aligned} \tag{2}$$

where Δt_e is the time step for the MMUT integrator. The density matrix is then propagated from time t_{k-1} to t_{k+1} with a fixed nuclear position

$$\mathbf{P}(t_{k+1}) = \mathbf{U}(t_k)\cdot\mathbf{P}(t_{k-1})\cdot\mathbf{U}^{\dagger}(t_k) \tag{3}$$

By computing the Kohn−Sham matrix at the midpoint of the step, the MMUT method accounts for linear changes in the density matrix during the time step. Because the electronic wave function changes much faster than the nuclear motion, the nuclear position coupled midpoint Fock/Kohn−Sham propagator updates integrals required in the Fock/Kohn−Sham matrix with the second kind of time step Δt_{Ne}, which encompasses $m\Delta t_e$ iterations. The integrals are recomputed at the midpoint of every Δt_{Ne} time step, $t' + (\Delta t_{Ne})/2$, and are used in the Fock/Kohn−Sham matrix $\mathbf{K}$ for the m MMUT steps between t' and $t' + \Delta t_{Ne}$

$$\mathbf{K}(t) = \mathbf{h}\left[x\left(t'+\frac{\Delta t_{Ne}}{2}\right)\right] + \mathbf{G}_{xe}\left[x\left(t'+\frac{\Delta t_{Ne}}{2}\right), \mathbf{P}(t)\right] \tag{4}$$

where $\mathbf{h}$ and $\mathbf{G}_{xe}$ are one and two electron matrices, respectively. The nuclear position is updated for $n\Delta t_{Ne}$ time steps before the gradient is recalculated, which occurs in the third time step $\Delta t_N = n\Delta t_{Ne}$. Velocity Verlet is used to propagate the nuclear coordinates

$$p(t_{k+1/2}) = p(t_k) - \frac{1}{2}g(t_k)\cdot\Delta t_N \tag{5}$$

$$x(t_{k+1}) = x(t_k) + \frac{p(t_{k+1/2})}{M}\cdot\Delta t_N \tag{6}$$

$$p(t_{k+1}) = p(t_{k+1/2}) - \frac{1}{2}g(t_{k+1})\cdot\Delta t_N \tag{7}$$

where p is the momenta and g is the energy gradient. The quantum mechanical gradient, for noncommuting Fock/Kohn−Sham and density matrices, $[\mathbf{K}, \mathbf{P}] \neq 0$, is generally different than that for Born−Oppenheimer dynamics.

In the current work, we extend the implementation to include the electric-dipole approximation in the Hamiltonian to describe instantaneous electron-field interactions

$$\mathbf{K}(t) = \mathbf{K}_0(t) + \mathbf{d}\cdot e(t) \tag{8}$$

where $\mathbf{K}_0$ is the field-free Fock/Kohn−Sham matrix, $d_{\mu\nu} = \langle\chi_\mu|r|\chi_\nu\rangle$ is the dipole integral in the AO basis, and we use a linearly polarized and spatially homogeneous external field of frequency ω and maximum field strength E_{max}

$$e(t) \approx E_{max}\cdot\sin(\omega\cdot t) \tag{9}$$

B. Boltzmann Ensemble of Initial Conditions. We simulate a Boltzmann ensemble of acetylene dication molecules at room temperature (298 K). For a specific vibrational mode with a given Boltzmann-sampled vibrational energy, the initial phase was chosen randomly and classically. The total angular momentum was set to zero. Since the actual potential energy surface is not strictly harmonic, the initial vibrational coordinates and momenta generated by this procedure were scaled to correct for the anharmonicity.[33] This ensemble assumes a broad geometric distribution of vibrational phases of the initial ground state ($^3\Sigma_g^-$) species from which the strong laser field interactions take place. A similar approach has been implemented for studies of Coulomb explosion of the acetylene dication.[29] A total of 50 initial conditions and trajectories were integrated for each set of applied field parameters. Figures 1a−c show the room temperature Boltzmann distribution of the initial conditions. The C−H bonds (Figure 1a) are within about ±0.15 Å of the equilibrium bond length of 1.14 Å. Because the C−C bond is stronger, the distribution (Figure 1b) is not as broad, with 95% within ±0.07 Å of the equilibrium of 1.35 Å. Even though the minimum energy geometry of $C_2H_2^{2+}$ is linear, vibrational Boltzmann sampling of the bending modes allows deviation from exact linearity. The initial distribution of the ∠H−C−C angle shown in Figure 1c indicates that 90% of the runs are within ±25° of the linear structure. In our simulations, fields are applied parallel and perpendicular to the axis described by the optimized linear structure, and this distribution indicates that most of the $C_2H_2^{2+}$ starting conditions give a structure that is close to linear.

III. Results and Discussion

The modified development version of the GAUSSIAN[34] series of programs, using the BLYP density functional and the 6-31++G(d,p) basis set, was used to carry out all computations in the present investigation. The ground state of the acetylene dication has a triplet configuration ($^3\Sigma_g^-$) with two unpaired electrons each occupying one π_u bonding orbital. Within our calculations, the molecular axis is along the z axis, and the two π bonds are aligned along the x and y axes. The ground-state optimized C−C bond length is 1.35 Å, and the C−H bond length is 1.14 Å. For the electronic excitations in the PESs, we use linear response time-dependent density functional theory as described in references 35 and 36. In the Ehrenfest dynamics, a step size of $t_N = 0.10$ fs is used for the velocity Verlet, t_{Ne}= 0.02 for the midpoint Kohn−Sham integrator, and $t_e = 0.002$ fs for the MMUT step. Tests showed that these time steps conserve the energy of the system (after field removal) to within

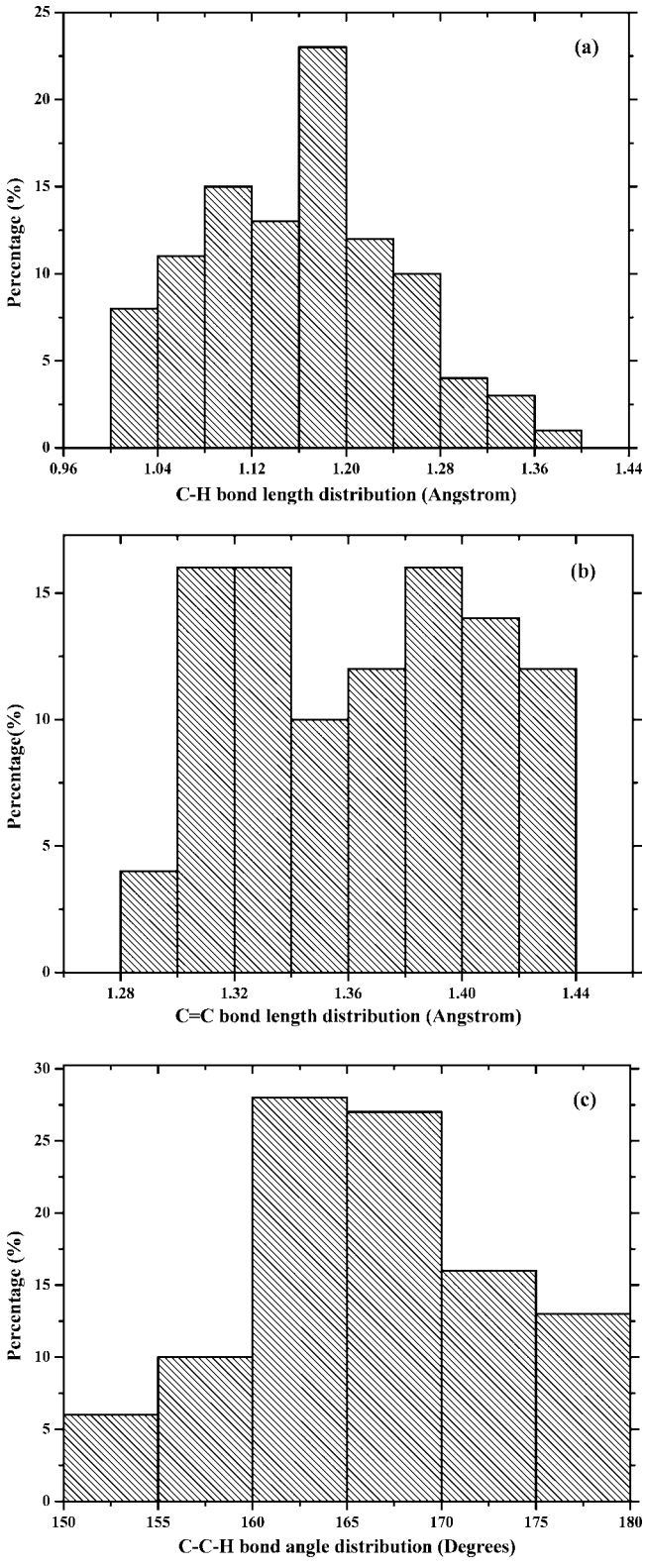

Figure 1. Boltzmann distribution of initial conditions: (a) initial C−H bond length, (b) initial C−C bond length, and (c) initial distribution of the ∠H−C−C angle.

10^{-4} hartree, and so represent a good combination of accuracy and computational cost.

For our Ehrenfest dynamics field parameters, we use a constant envelope ∼20 fs laser pulse, with $E_{max} = 0.08$ au (which corresponds to a field intensity of 2×10^{14} W/cm^2). After the first 20 fs when the laser field is on, the molecular reaction continues until $t = 150$ fs. At the end of the simulation, the C−H and C−C bonds are considered broken if their length exceeds 3 Å. We divide our nonadiabatic Ehrenfest molecular dynamics results into five dissociation pathways:

(1) no bonds are broken

(2) single-proton dissociation

$$C_2H_2^{2+} \rightarrow C_2H^+ + H^+$$

(3) dissociation of both C−H bonds

$$C_2H_2^{2+} \rightarrow C_2^+ + H + H^+ \quad \text{and} \quad C_2H_2^{2+} \rightarrow C_2 + H^+ + H^+$$

(4) dissociation of all bonds

$$C_2H_2^{2+} \rightarrow C + C + H^+ + H^+$$

(5) proton dissociation with C−C dissociation

$$C_2H_2^{2+} \rightarrow CH^+ + C + H^+$$

An additional pathway, with the C−C bond breaking with no C−H dissociation, is possible but was never observed in our simulations of the triplet state. Although a large torsional energy could break the C−C bond, the Boltzmann sampling shows that this mechanism is very unlikely at room temperature. This pathway is thought to occur through an excited singlet surface through a bent transition state.[24] Although vibrational sampling of the bending mode breaks the strict linear symmetry of the optimized structure, the results of our simulations can be broadly divided into two different categories: laser application perpendicular to the molecular axis and laser application along the molecular axis. Although this division is made for the ease of interpreting our theoretical results, intense laser pulses can be used to produce alignment of even nonpolar molecules, with the molecule aligning with its most polarizable axis along the laser polarization direction.[37−40] Within our scheme, this technique could be used to provide greater control of the molecular dissociation.

A. Nonadiabatic Ehrenfest Molecular Dynamics with the Field Perpendicular to the Molecular Axis. When a 20 fs laser pulse was applied in the *xy* plane (perpendicular to the molecular *z* axis, with $E_{max} = 0.057$ au along both the *x* and *y* axes), no bonds were broken within the experimentally relevant range of photon energies 1.5 eV = 800 nm (titanium−sapphire laser) to 8.3 eV = 157 nm (an ArF excimer laser, the high-energy range of current laser technology). We increased the photon energy and found that no bonds broke until we reached an extremely high photon energy of 13.6 eV = 91.2 nm. This high-energy field frequency did not lend itself to controlled dissociation, however, as there were many dissociation pathways accessed, but none of them dominant.

With the 13.6 eV photon energy *xy* field, the distribution of the five dissociation pathways is shown in Figure 2. The percentages range from 10% (pathway 5: dissociation of a single C−H bond with C−C dissociation) to 30% (pathway 3: dissociation of both C−H bonds). Thus, when the laser field is aligned perpendicular to the molecular axis, the probability of controlling molecular dissociation of $C_2H_2^{2+}$ is rather small.

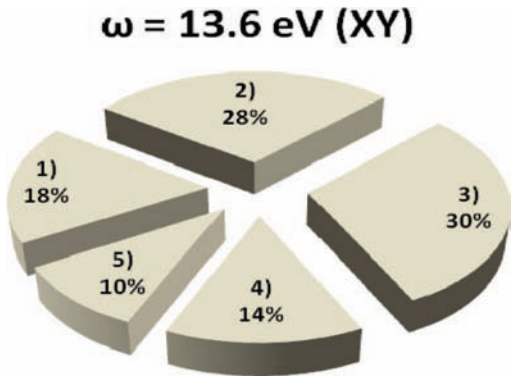

Figure 2. Percentages of various dissociation pathways with an *xy* laser field with a frequency of $\omega = 13.6$ eV. The five different pathways are (1) no bonds are broken; (2) single-proton dissociation, $C_2H_2^{2+} \rightarrow C_2H^+ + H^+$; (3) dissociation of both C−H bonds, $C_2H_2^{2+} \rightarrow C_2^+ + H + H^+$ and $C_2H_2^{2+} \rightarrow C_2 + H^+ + H^+$; (4) dissociation of all bonds, $C_2H_2^{2+} \rightarrow C + C + H^+ + H^+$; (5) proton dissociation with C═C dissociation, $C_2H_2^{2+} \rightarrow CH^+ + C + H^+$.

We next analyze the corresponding *xy*-allowed excited states. Figures 3a and 3b show the PESs for the four lowest energy *xy*-dipole-allowed electronic transitions as functions of C−H and C−C distances, respectively, as well as the PES of the ground state. For the PESs in Figure 3a, the C−H bonds were symmetrically stretched. The vertical lines indicate the maximum and minimum starting bond lengths in the Boltzmann ensemble. The two lowest lying excited states in Figures 3a and 3b correspond to excitation from the C−H bonding σ_g orbital to the C−C bonding π_u orbital, which should weaken the C−H bond and meanwhile strengthen the C−C bond. The lowest energy excited state should be accessible with a field frequency ω of ∼5 eV = 248 nm when the field is aligned in the *xy* plane. Although it seems that this excitation provides a desirable control scheme for selective bond breakage since it weakens the C−H bond while strengthening the C−C bond, these $\sigma \rightarrow \pi$ transitions are only weakly allowed in the *xy* plane (oscillator strength $f < 0.004$), even at stretched bond lengths. The second highest *xy*-allowed excited state is also very weakly allowed.

The two higher energy excitations in Figures 3a and 3b correspond to excitations from the C−H bonding σ_g orbital to the C−C antibonding π_g orbital, which weakens both the C−H and C−C bonds. While transitions to these states are not highly allowed, the oscillator strength of the fourth excited state, at ∼14 eV, is a bit larger than the other *xy* states; it ranges between $f = 0.2$ and 0.03, indicating that population of this state is likely responsible for the dissociations observed with the 13.6 eV field. In addition to this state having a nonminimal oscillator strength, it is also seen to be repulsive along both the C−C and C−H bond coordinates, allowing for direct dissociation. We thus see that while the first of the *xy* transitions is in the experimental photon energy range, the very small oscillator strength of this state keeps it from being available to $C_2H_2^{2+}$ upon excitation with an applied laser field. Population of a higher lying state, at an energy well beyond the reach of today's experimental laser technology, is theoretically possible due to a larger oscillator strength. It appears to be this repulsive state that causes the various dissociations seen in Figure 2.

B. Nonadiabatic Ehrenfest Molecular Dynamics with the Field Parallel to the Molecular Axis. When the laser field is aligned along the molecular *z* axis, there is a wide range of dissociation patterns observed. Figure 4 shows the distribution of the various five pathways for four different photon energies.

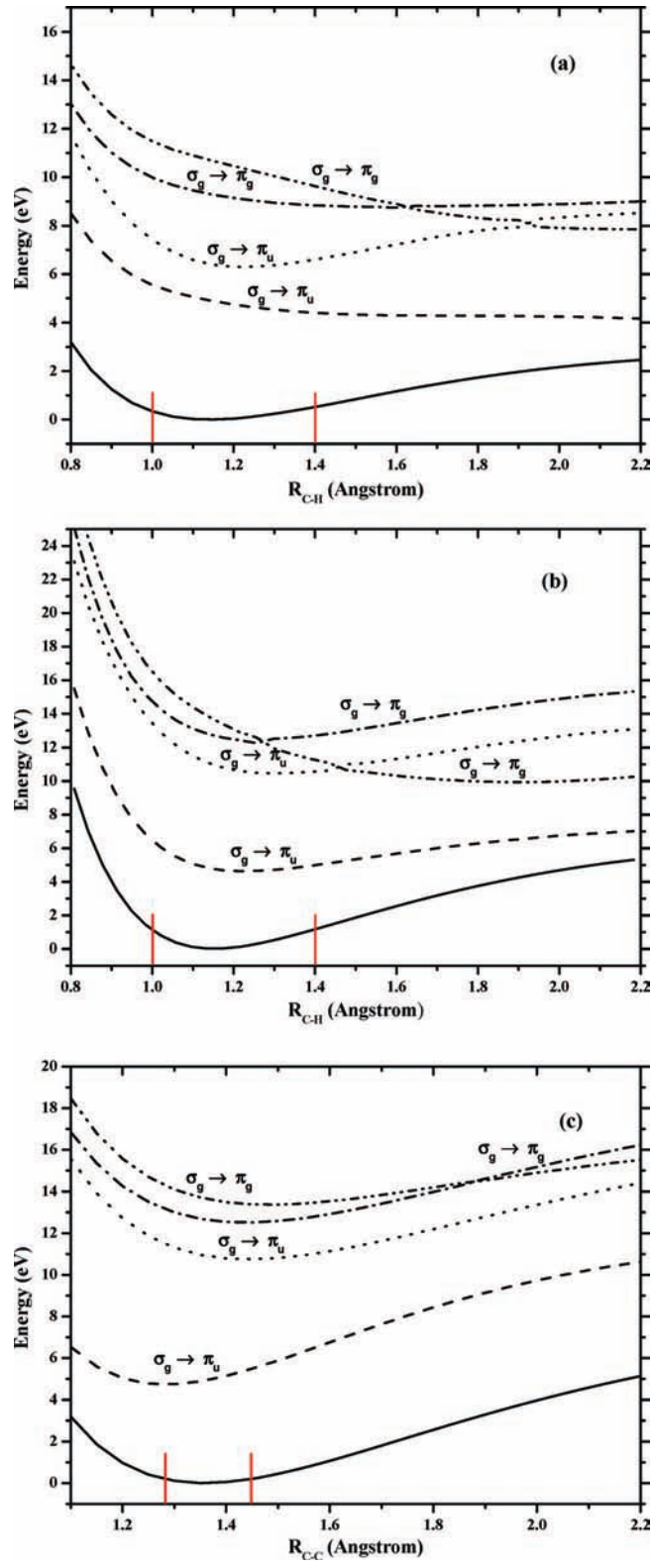

Figure 3. Potential energy surfaces for $C_2H_2^{2+}$. Red lines indicate the range of bond lengths within the room temperature Boltzmann distribution: (a) *xy*- allowed states for the asymmetric C−H stretch; one C−H bond is stretched while the other is optimized, (b) *xy*-allowed states for the symmetric C−H stretch; both C−H bonds have the same length, and (c) *xy*-allowed states for the C−C stretch.

In all tested laser fields, the C−H dissociation channels (pathways 2 and 3) are the most probable reaction pathways. At the lowest photon energy, 9.5 eV, single C−H dissociation, pathway 2, is the dominant dissociation channel. When the

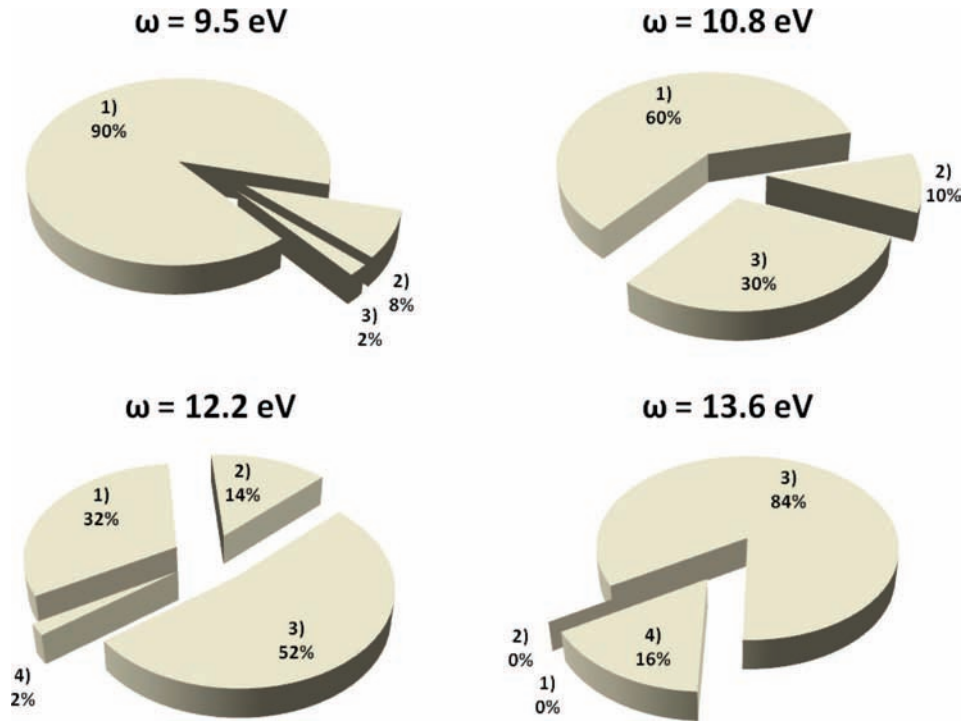

Figure 4. Percentages of various dissociation pathways with a z laser field. The five different pathways are given in Figure 2 and in the text.

photon energy increases, the probability of double C−H bond dissociation, pathway 3, also increases. The Ehrenfest trajectories at the lower photon energies (<12 eV) do not undergo C−C dissociation. When the photon energy is above 12 eV, the C−C dissociation channel is open; however, these higher photon energies also lead to C−H dissociation. Therefore, a simple frequency control scheme as explored here on the triplet surface is not able to break the C−C bond while maintaining the C−H bonds, but at a frequency of 9.5 eV, we are, in fact, able to selectively break only one of the C−H bonds since pathway 2 dominates over pathway 3. At higher frequencies, the double C−H dissociation of pathway 3 dominates. Examination of the energy profiles during the dynamics indicates that trajectories with a 10 eV or greater increase in the potential energy when the field is on are likely to experience dissociation. As the dynamics continue, some of this large potential energy is transferred to the kinetic energy of the $C_2H_2^{2+}$ fragments.

With double C−H dissociation, we find that the charge profile of the fragments varies with laser frequency. Since Ehrenfest dynamics propagates the nuclear motion on an average potential energy surface, the final partial charge indicates probabilities of dissociation on various surfaces. At higher frequencies, we find that each hydrogen has a larger positive charge, with the C_2 fragment holding onto the positive charge more with the lower 10.8 eV frequency. This means that higher frequency laser fields are more likely to lead to double-proton dissociation, while lower frequency laser fields are more likely to lead to single-proton dissociation, followed by dissociation of neutral hydrogen.

Figure 5 shows representative natural charge distributions during the dynamics for a single set of initial conditions for both the low-frequency (10.8 eV) and high-frequency (13.6 eV) fields. The figure shows that, for both frequencies, positive charge migrates toward the hydrogens. Oscillation of charge continues after the field is removed at 20 fs, mostly seen in the charges of the two carbons in the C_2 fragment. However, even with this charge oscillation on one fragment, the overall charge on C_2 remains fairly constant. This charge oscillation indicates a mixing of excited states with the ground-state PES, where

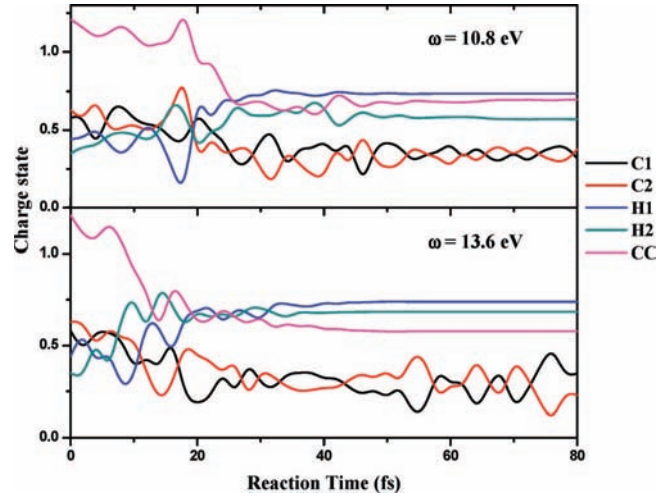

Figure 5. Time-dependent charge distribution of a representative trajectory in an $\omega = 10.8$ eV and $\omega = 13.6$ eV field. Atom C1 connects with H1 and C2 with H2. The sum of the charge on C1 and C2 is given by the CC line.

the excited states and ground state have differing charge character. The difference in the final charge distribution for the two frequencies can be correlated to the timing for the C−H bond breakage. For the 10.8 eV field, the first C−H dissociation occurs after the field is off, at ~27 fs, with subsequent dissociation of the other C−H bond at 36 fs. The 13.6 eV field breaks the first C−H bond at 17 fs, followed by quick dissociation of the other C−H bond at 21 fs. This much faster dissociation does not allow the positive charge to reequilibrate onto the remaining C_2H fragment after the initial bond breakage, which causes the second proton to leave with more positive charge.

As with the perpendicular xy laser field, we rationalize these dissociation patterns through analysis of the electronic excitations. Figures 6a−c are the PESs for z-allowed transitions for symmetric and asymmetric C−H bond breakage and C−C bond

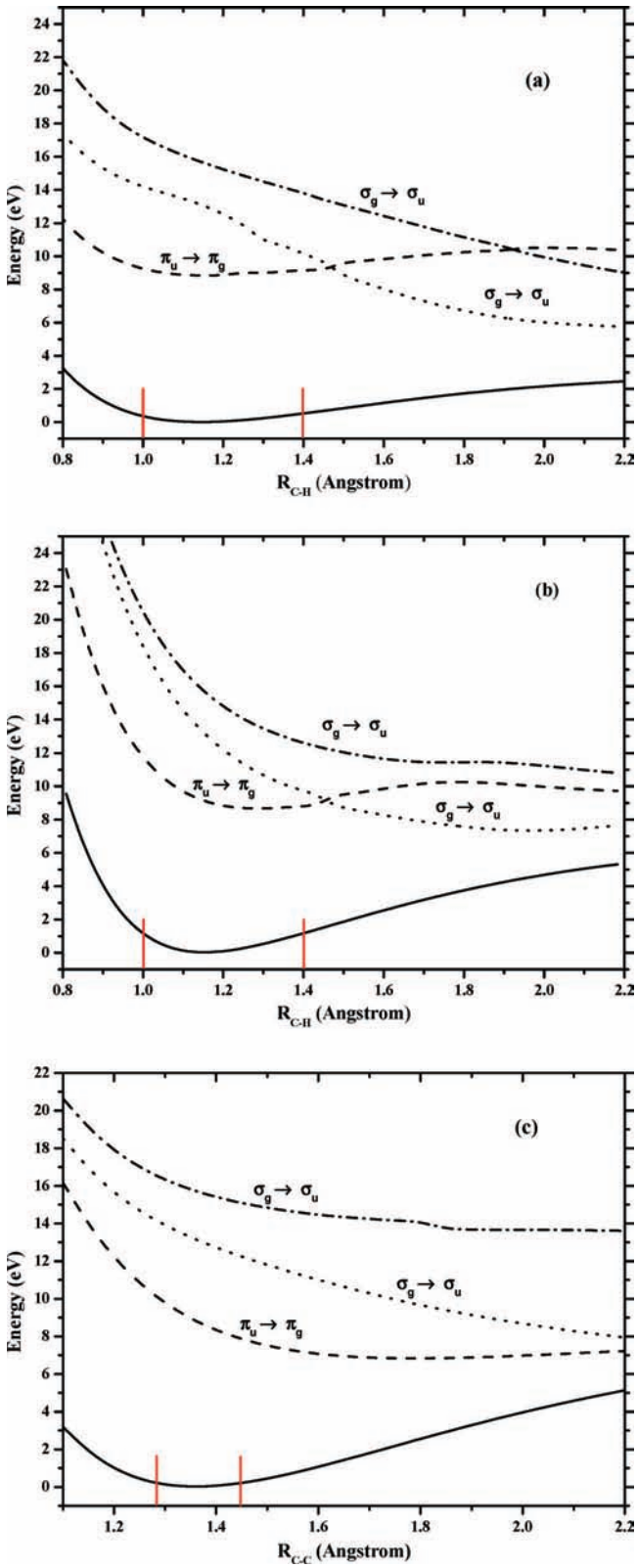

Figure 6. Potential energy surfaces for $C_2H_2^{2+}$. Red lines indicate the range of bond lengths within the room temperature Boltzmann distribution. Bond lengths are in angstrom: (a) *z*-allowed states for the asymmetric C−H stretch; one C−H bond is stretched while the other is optimized, (b) *z*-allowed states for the symmetric C−H stretch; both C−H bonds have the same length, and (c) *z*-allowed states for the C−C stretch.

breakage. The lowest energy excited state is *z*-dipole-allowed; the oscillator strength *f* ranges from 0.2 to 0.4 within the initial Boltzmann geometries (marked with a vertical line). This lowest energy state corresponds to excitation from the C−C π_u bonding orbital to the C−C π_g* antibonding orbital, which should lead to C−C bond weakening followed by a possible dissociation. Along the C−H coordinate this first excited state has a shallow potential well, while along the C−C coordinate the PES is very flat. The second and third excited-state PESs in Figures 6a−c correspond to excitation from the C−H bonding σ_g orbital to the C−H antibonding σ_u* orbital. This kind of excitation will result in a zero C−H bond order and is observed to have a repulsive PES along both the C−H and C−C bond coordinates. While the second excited state has a small oscillator strength ($f = 0.02-0.04$), the third excited state is highly allowed: *f* ranges between 0.6 and 1.1 within the initial Boltzmann geometries.

Figure 6 suggests that within the thermally sampled distances (Figures 1b and 1c), photon energies of ∼8−11 eV can excite $C_2H_2^{2+}$ to the first excited state, which should weaken the C−C bond. However, the lower energy field frequencies at 9.5 and 10.8 eV do not cause any dissociation of the C−C bond within the Ehrenfest dynamics; only C−H dissociation is observed. This is likely due to the small potential well of the first excited state, which makes the PES not entirely repulsive, thus not allowing for immediate dissociation of the C−C bond.

While we can rationalize the observance of the C−H dissociation at low photon frequencies of 9.5 and 10.8 eV by realizing that the second excited state becomes energetically available at these photon frequencies at highly stretched C−H distances (see Figure 6a, b), this rationale was surprising initially, considering the relatively small oscillator strength of this state compared to the first excited state. However, the oscillator strength of the second excited state is still greater than the fourth *xy*-allowed state that caused dissociation with the 13.6 eV field in the *xy* direction. It appears that in addition to requiring a nonminimal oscillator strength ($f > 0.01$), dissociation dynamics also prefers the shape of the PES to be repulsive, so that direct dissociation can occur. Thus, at these lower energy frequencies, it is the repulsive nature of PES that determines the dynamics, rather than the magnitude of the oscillator strength.

An additional question in understanding the Ehrenfest dynamics results is why single C−H bond breakage (pathway 2) dominates double C−H bond breakage (pathway 3) at the lowest photon energy. Close scrutiny of the symmetric and asymmetric C−H PESs shows that the second excited state, which we have shown is responsible for the dissociation dynamics at these lower energies, dips to slightly lower energies for the antisymmetric stretching of the C−H bond, compared to the symmetric stretching. We see that this selectivity for single C−H dissociation is suppressed by increasing the photon energy. This result agrees well with our phase analysis of initial conditions in which asymmetric stretch is slightly more probable than the symmetric stretch.

Going to even higher photon energies at 12.2 and 13.6 eV shows that favoring of single C−H bond breakage (pathway 2) over double C−H bond breakage (pathway 3) decreases as the system acquires more energy. Overall, a greater percentage of C−H dissociation is observed, which is likely due to $C_2H_2^{2+}$ now having enough energy to access the highly allowed and repulsive third excited state. In addition, some complete dissociation is seen, including the C−C bond. This indicates that the extra energy of the field allows the system to overcome the potential barrier seen in the PES of the first excited state, allowing for complete, direct dissociation of all bonds.

IV. Conclusion

We have extended our TDDFT Ehrenfest dynamics technique to include the effects of an applied laser field. In this work, we have used this technique to study the laser-controlled dissociation of the acetylene dication, $C_2H_2^{2+}$. The acetylene dication is one of the simplest stable dications, and its symmetry makes it particularly instructional in exploring various aspects of laser-controlled dissociation. Our dynamics results with various field directions and field frequencies show several interesting phenomena. When the field is applied perpendicular to the molecular axis, dissociation only occurs at a high photon energy: 13.6 eV, with no one dominant dissociation pathway. When the field is applied parallel to the molecular axis, dissociation occurs at lower energies with the branching ratios of the dissociation products differing for each frequency studied. For the lowest frequency, 9.5 eV, we observe 10% of trajectories undergoing C−H dissociation, with selective dissociation of a single C−H bond over dissociation of both C−H bonds, with single C−H bond dissociation being favored by 4:1. This selective dissociation disappears at higher photon energies, where dissociation of both C−H bonds becomes the dominant pathway. The amount of dissociation increases as the frequency is increased: 40% of trajectories involve C−H bond breakage at 10.8 eV, 68% at 12.2 eV, and 100% at 13.6 eV. At 13.6 eV, 16% of the trajectories undergo complete dissociation, breaking all bonds in $C_2H_2^{2+}$.

The results of our Ehrenfest dynamics are analyzed in terms of the excited-state PESs along the C−H and C−C bond coordinates for both *xy*-allowed (perpendicular to molecular axis) and the *z*-allowed (parallel to molecular axis) excited states. The high-energy 13.6 eV field is required in the perpendicular direction because the lower energy excited states have very small oscillator strengths. It is not until a repulsive surface with an oscillator strength large enough (f for this third excited state ranges between 0.2 and 0.03) becomes energetically accessible that dissociation occurs. It is thus extremely difficult to control bond breakage via states with very small oscillator strengths. The PES analysis of the *z*-allowed states shows that the first excited state, which corresponds to weakening the C−C bond, has a moderate oscillator strength. However, because this state has a shallow potential well and so is not entirely repulsive, we do not observe direct C−C dissociation at energies corresponding to this state. Higher field energies allow $C_2H_2^{2+}$ enough extra energy to overcome the potential barrier and dissociate along this PES. The second excited *z*-allowed state has a small oscillator strength ($f = 0.02-0.04$), comparable to the dissociative *xy*-allowed state, but is highly repulsive. We thus determined that this state was responsible for the low-energy C−H direct dissociations. This state has a slightly lower energy along the C−H antisymmetric stretching coordinate than along the C−H symmetric stretching coordinate, thus explaining the observed 4:1 preference for single C−H dissociation over double C−H dissociation in the Ehrenfest dynamics at low-energy 9.5 eV frequencies. The third *z*-allowed excited state is repulsive and has a large oscillator strength ($f > 1$) and is thus likely responsible for the large percentage of dissociations seen at the higher energy frequencies.

Acknowledgment. This work is supported by the National Science Foundation (PHY-CDI 0835543), ACS Petroleum Research Fund (46487-G6), and Gaussian Inc.

References and Notes

(1) Zewail, A. H. *J. Phys. Chem. A* **2000**, *104*, 5660.
(2) Rice, S.; Zhao, M. *Optical control of molecular dynamics*; Wiley Interscience: New York, 2000.
(3) Shapiro, M.; Brumer, P. W. *Principles of the Quantum Control of Molecular Processes*; Wiley Interscience: New York, 003.
(4) Padgett, M.; Allen, L. *Phys. World* **1997**, *10*, 35.
(5) Levis, R. J.; Menkir, G. M.; Rabitz, H. *Science* **2001**, *292*, 709.
(6) Bardeen, C. J.; Yakovlev, V. V.; Wilson, K. R.; Carpenter, S. D.; Weber, P. M.; Warren, W. S. *Chem. Phys. Lett.* **1997**, *280*, 151.
(7) Kleiman, V. D.; Arrivo, S. M.; Melinger, J. S.; Heilweil, E. *J. Chem. Phys.* **1998**, *233*, 207.
(8) Pastirk, I.; Brown, E. J.; Zhang, Q. G.; Dantus, M. *J. Chem. Phys.* **1998**, *108*, 4375.
(9) Yakovlev, V. V.; Bardeen, C. J.; Che, J. W.; Cao, J. S.; Wilson, K. R. *J. Chem. Phys.* **1998**, *108*, 2309.
(10) Legare, F.; Chelkowski, S.; Bandrauk, A. D. *Chem. Phys. Lett.* **2000**, *329*, 469.
(11) Chelkowski, S.; Bandrauk, A. D. *J. Chem. Phys.* **1993**, *99*, 4279.
(12) Elliott, D. J.; Townsend, P. D. *Philos. Mag.* **1971**, *23*, 261.
(13) Hattori, K.; Okano, A.; Nakai, Y.; Itoh, N. *Phys. Rev. B* **1992**, *45*, 8424.
(14) Nakai, Y.; Hattori, K.; Okano, A.; Taguchi, T.; Kanasaki, J.; Itoh, N. *Surf. Sci.* **1993**, *283*, 169.
(15) Kanasaki, J.; Ishida, T.; Ishikawa, K.; Tanimura, K. *Phys. Rev. Lett.* **1998**, *80*, 4080.
(16) Hess, W. P.; Joly, A. G.; Beck, K. M.; Henyk, M.; Sushko, P. V.; Trevisanutto, P. E.; Shluger, A. L. *J. Phys. Chem. B* **2005**, *109*, 19563.
(17) Dantus, M. *Annu. Rev. Phys. Chem.* **2001**, *52*, 639.
(18) Gauduel, Y. *Actual. Chim.* **2001**, 3.
(19) Li, X.; Tully, J. C.; Schlegel, H. B.; Frisch, M. J. *J. Chem. Phys.* **2005**, 123.
(20) Kinugawa, T.; Lablanquie, P.; Penent, F.; Palaudoux, J.; Eland, J. H. D. *J. Electron Spectrosc. Relat. Phenom.* **2004**, *141*, 143.
(21) Hishikawa, A.; Matsuda, A.; Fushitani, M.; Takahashi, E. J. *Phys. Rev. Lett.* **2007**, 99.
(22) Osipov, T.; Cocke, C. L.; Prior, M. H.; Landers, A.; Weber, T.; Jagutzki, O.; Schmidt, L.; Schmidt-Bocking, H.; Dorner, R. *Phys. Rev. Lett.* **2003**, 90.
(23) Pople, J. A.; Frisch, M. J.; Raghavachari, K.; Schleyer, P. V. *J. Comput. Chem.* **1982**, *3*, 468.
(24) Duflot, D.; Robbe, J. M.; Flament, J. P. *J. Chem. Phys.* **1995**, *102*, 355.
(25) Thissen, R.; Delwiche, J.; Robbe, J. M.; Duflot, D.; Flament, J. P.; Eland, J. H. D. *J. Chem. Phys.* **1993**, *99*, 6590.
(26) Mebel, A. M.; Zyubina, T. S.; Dyakov, Y. A.; Bandrauk, A. D.; Lin, S. H. *Int. J. Quantum Chem.* **2005**, *102*, 506.
(27) Zyubina, T. S.; Dyakov, Y. A.; Lin, S. H.; Bandrauk, A. D.; Mebel, A. M. *J. Chem. Phys.* **2005**, 123.
(28) Palaudoux, J.; Hochlaf, M. *J. Chem. Phys.* **2007**, 126.
(29) Li, X.; Bernhard, H. *J. Phys. Chem. A* **2004**, *108*, 468.
(30) Isborn, C. M.; Li, X. S.; Tully, J. C. *J. Chem. Phys.* **2007**, 126.
(31) Li, X.; Smith, S. M.; Markevitch, A. N.; Romanov, D. A.; Levis, R. J.; Schlegel, H. B. *Phys. Chem. Chem. Phys.* **2005**, *7*, 233.
(32) Verlet, L. *Phys. Rev.* **1967**, *159*, 98.
(33) Hase, W. L. Classical Trajectory Simulations: Initial Conditions. In *Encyclopedia of Computational Chemistry*; Schleyer, P. v. R., Allinger, N. L., Clark, T., Gasteiger, J., Kollman, P. A., Schaefer, H. F., III; Schreiner, P. R., Eds.; Wiley: New York, 1998; p 402.
(34) Frisch, M. J.; Trucks, G. W.; Schlegel, H. B.; Scuseria, G. E.; Robb, M. A.; Cheeseman, J. R.; Montgomery, J. A., Jr.; Vreven, T.; Kudin, K. N.; Burant, J. C.; Millam, J. M.; Iyengar, S. S.; Tomasi, J.; Barone, V.; Mennucci, B.; Cossi, M.; Scalmani, G.; Rega, N.; Petersson, G. A.; Nakatsuji, H.; Hada, M.; Ehara, M.; Toyota, K.; Fukuda, R.; Hasegawa, J.; Ishida, M.; Nakajima, T.; Honda, Y.; Kitao, O.; Nakai, H.; Klene, M.; Li, X.; Knox, J. E.; Hratchian, H. P.; Cross, J. B.; Adamo, C.; Jaramillo, J.; Gomperts, R.; Stratmann, R. E.; Cammi, R.; Pomelli, C.; Ochterski, J. W.; Ayala, P. Y.; Morokuma, K.; Salvador, P.; Dannenberg, J. J.; Zakrzewski, V. G.; Dapprich, S.; Daniels, A. D.; Strain, M. C.; Farkas, O.; Malick, D. K.; Rabuck, A. D.; Raghavachari, K.; Foresman, J. B.; Ortiz, J. V.; Cui, Q.; Baboul, A. G.; Clifford, S.; Cioslowski, J.; Stefanov, B. B.; Liu, G.; Liashenko, A.; Piskorz, P.; Komaromi, I.; Martin, R. L.; Fox, D. J.; Keith, T.; Al-Laham, M. A.; Peng, C. Y.; Nanayakkara, A.; Challacombe, M.; Gill, P. M. W.; Johnson, B.; Chen, W.; Wong, M. W.; Gonzalez, C.; Pople, J. A. Gaussian 01 (Development Version); Gaussian, Inc.: Pittsburgh, PA, 2002.
(35) Gill, P. M. W.; Gordon, M. S.; Head-Gordon, M.; Radom, L. *J. Chem. Phys.* **2004**, *120*, 9445.
(36) Stratmann, R. E.; Scuseria, G. E.; Frisch, M. J. *J. Chem. Phys.* **1998**, *109*, 8218.
(37) Friedrich, B.; Herschbach, D. *Phys. Rev. Lett.* **1995**, *74*, 4623.
(38) Kim, W.; Felker, P. M. *J. Chem. Phys.* **1996**, *104*, 1147.
(39) Seideman, T. *J. Chem. Phys.* **1995**, *103*, 7887.
(40) Sakai, H.; Safvan, C. P.; Larsen, J. J.; Hilligsoe, K. M.; Hald, K.; Stapelfeldt, H. *J. Chem. Phys.* **1999**, *110*, 10235.

JP811431U